

## Electron emission from films of Ag and Au nanoparticles excited by a femtosecond pump-probe laser

A. Gloskovskii,<sup>1</sup> D. A. Valdaitsev,<sup>1</sup> M. Cinchetti,<sup>2</sup> S. A. Nepijko,<sup>1,3,\*</sup> J. Lange,<sup>2</sup> M. Aeschlimann,<sup>2</sup> M. Bauer,<sup>4</sup> M. Klimenkov,<sup>5</sup> L. V. Viduta,<sup>3</sup> P. M. Tomchuk,<sup>3</sup> and G. Schönhense<sup>1</sup>

<sup>1</sup>*Institute of Physics, University Mainz, Staudingerweg 7, 55099 Mainz, Germany*

<sup>2</sup>*Department of Physics, University Kaiserslautern, 67663 Kaiserslautern, Germany*

<sup>3</sup>*Institute of Physics, National Academy of Sciences of Ukraine, pr. Nauki 46, 03028 Kiev, C.I.S./Ukraine*

<sup>4</sup>*Institute of Experimental and Applied Physics, University Kiel, Leibnizstr. 19, 24118 Kiel, Germany*

<sup>5</sup>*Institute for Materials Research I, Forschungszentrum Karlsruhe, Hermann-von-Helmholtz-Platz 1, vacc76344 Eggenstein-Leopoldshafen, Germany*

(Received 15 June 2007; revised manuscript received 2 April 2008; published 19 May 2008)

Electron emission from Ag and Au nanoparticle films was studied under excitation with femtosecond-laser pulses with photon energies of 1.55 and 3.1 eV. Films were grown on a glass substrate with particle sizes from the nanometer range to a continuous layer. The transition from a continuous film to a nanoparticle film is accompanied by an increase in photoemission current by more than an order of magnitude. Pump-and-probe experiments with variable delay gave information on the lifetime of the intermediate states. At a fixed pulse power, the emission yield increases as the temporal width of the laser pulses is decreased. Experimental results are interpreted in terms of two different electron emission mechanisms, i.e., multiphoton photoemission and thermionic emission or thermally assisted multiphoton photoemission. The first mechanism prevails for continuous films and larger particles with sizes above several tens of nanometers; the second one prevails for smaller nanoparticles with sizes of a few nanometers.

DOI: [10.1103/PhysRevB.77.195427](https://doi.org/10.1103/PhysRevB.77.195427)

PACS number(s): 78.67.Bf, 79.20.Ds, 79.40.+z, 79.60.-i

### I. INTRODUCTION

The study of photoemission from small metal particles at femtosecond-laser excitation is of high interest for basic and applied research. The feasibility of studying the electron dynamics (relaxation and charge transfer) as a function of band structure, spin polarization, surface morphology, and dimensionality was demonstrated in Refs. 1 and 2. The femtosecond imaging of surface plasmon dynamics in a nanostructured Ag film was presented in Ref. 3.

In our previous work,<sup>4</sup> we described results for Ag films on a Si(111) surface obtained by means of time-resolved (time-of-flight) photoemission electron microscopy (PEEM) by using femtosecond-laser radiation with a relatively large pulse width ( $\sim 200$  fs) with photon energies below the work function of Ag ( $h\nu < \phi$ ). Spatially resolved spectroscopy revealed that at the transition from a continuous Ag film to a Ag nanoparticle film, the intensity of the photoelectron emission increases by several orders of magnitude, and that their energy spectra are substantially different. This work gave evidence of two-photon photoemission (2PPE) as a dominant electron emission mechanism for particle sizes of typically 40 nm.

In the current study, we performed experiments by using shorter laser pulses ( $\geq 18$  fs) in a pump-probe setup, giving access to the mechanism of photoelectron emission from smaller metal nanoparticles in the size regime of a few nanometers. The studies were performed on films of Ag and Au particles on glass substrates with their size varying from  $< 1$  nm to a continuous film. The cluster structure and size distribution were analyzed by atomic force microscopy (AFM) and transmission electron microscopy (TEM) as well as high-resolution TEM (HRTEM). The photon energy, ra-

diation power, pulse duration, etc., were varied.

Our results show that different mechanisms have to be distinguished in the case of femtosecond-laser-induced photoemission from Ag nanoparticles. For large nanoparticles ( $> 40$  nm), two- and multiphoton photoemission is again identified as the dominating process. For small-sized particles, observed photoemission characteristics clearly point to the thermally assisted processes. The appearance of this excitation channel in this size regime is interpreted in terms of an efficient decoupling of an electronic and a phononic subsystem in very small nanoparticles, giving rise to a transient heatup of the electron gas on the subpicosecond time scales.

### II. EXPERIMENTAL DETAILS

Silver films with a wedge-shaped thickness profile have been prepared on a glass substrate. The substrate was manufactured from Uviol glass that is transparent in the visible and ultraviolet ranges. It had a round shape, with a diameter of  $D = 36$  mm. It served as a window in a glass vacuum device (see Fig. 1, right side). The device was pumped by a sublimation pump reaching a base vacuum of  $1 \times 10^{-8}$  mbar. A Ag film was immediately prepared before the measurements by using a thermal evaporator. This was placed at a distance of  $h = 7.5$  mm from the substrate and close to its lower edge. As a result, the distance from the evaporator to different areas of the substrate varied from  $h$  at its lower edge to  $l = \sqrt{h^2 + D^2}$  at the upper edge (see Fig. 1, right side). In addition to the distance, the angle of incidence  $\alpha$  also varies. This geometry allowed us to obtain a metal film, along which the mass thickness varied by a factor of 100. The growth rate at the region of maximum thickness was approximately equal to 0.03 nm/s. The substrate was

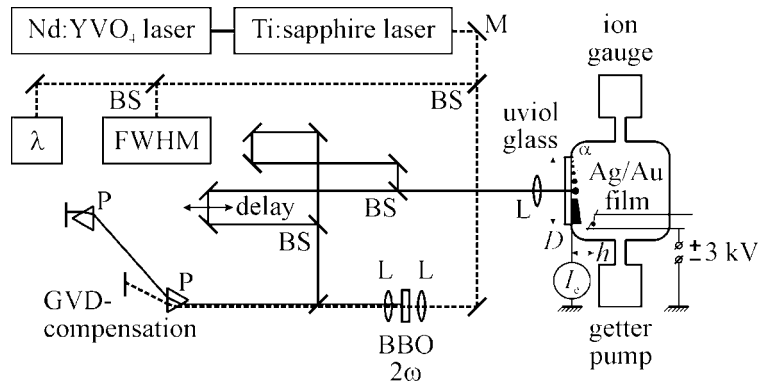


FIG. 1. Schematic view of the experimental setup. The dashed line marks the path of the output of the Ti:sapphire laser; the thin solid line corresponds to the frequency-doubled light. L, lens; M, mirror; BS, semitransparent mirror (beam splitter); P, prism;  $\lambda$  and FWHM, devices for the measurements of the wavelength and the width of the laser pulse.  $D$  is the diameter of the window,  $h$  is the distance from its inner face to the evaporator, and  $\alpha$  is the angle between the direction to the evaporator and the surface normal of the Ag film plane. Other designations are explained in the text.

kept at room temperature. The particle sizes were measured after finishing the emission measurements by means of an atomic force microscope (SIS Nanostation) and a high-resolution transmission electron microscope (Hitachi-8100). For characterization of the Ag films with the second method, nine copper TEM grids of 3 mm in diameter covered with a continuous amorphous carbon film of  $\sim 10$  nm thickness were attached to the substrate along the direction of the mass thickness gradient. The grids were characterized by a sufficient mechanical strength and transparency for the electrons used in the transmission electron microscope with 200 keV beam energy. HRTEM and AFM measurements in combination provided a lateral resolution of 0.12 nm and a resolution in the direction perpendicular to the substrate surface of about 0.01 nm, respectively. Au films were prepared in a second similar device.

After preparation of the film, the evaporator was used as collector of the emitted electrons by applying a potential of +3 kV. For measurements of the emission current, the sample (Ag and Au film) was grounded, and the incident laser beam was focused on it. A scheme of the experimental setup is shown in Fig. 1. The photoelectrons were excited by illuminating the substrate from the back (outer) side. The spot of the illuminating radiation with diameter at  $\sim 100 \mu\text{m}$  was scanned along the Ag and Au films in the direction of its mass thickness gradient. For all measurements, the radiation was purely  $s$ -polarized with respect to the substrate surface. Repeatability of the experimental results indicates that the structure of the Ag and Au films being studied remained unchanged at different modes of excitation. For comparison with common one-photon photoemission (1PPE), the continuous radiation of a high-pressure Hg lamp (power of 100 W, photon energy  $\leq 5.1$  eV) was used.

The laser system used for the experiments was a commercial mode-locked Ti:sapphire laser, which was pumped by about 7 W from a diode pumped all-solid-state laser system (Fig. 1, left side). It delivers pulses of up to 7.5 nJ/pulse with a full width at half maximum (FWHM) of 18 fs and a repetition rate of 82 MHz. The wavelength was 800 nm, corresponding to a photon energy of 1.55 eV (infrared). The lin-

early polarized output of the Ti:sapphire laser could be frequency doubled in a 0.2 mm thick beta barium borate (BBO) crystal to produce pulses with photon energy of 3.1 eV (blue). The conversion rate of the BBO is about 15%, giving pulse energies of up to 1.2 nJ and a FWHM of 27 fs. The maximum average powers were 600 and 100 mW for the infrared and blue laser beams, respectively. The pulse width could be continuously varied up to values of 500 fs by detuning the group velocity dispersion (GVD) compensator consisting of a pair of fused silica prisms. For the time-resolved (pump-probe) experiment, the laser pulses were split by a beam splitter to equal intensity of the pump-and-

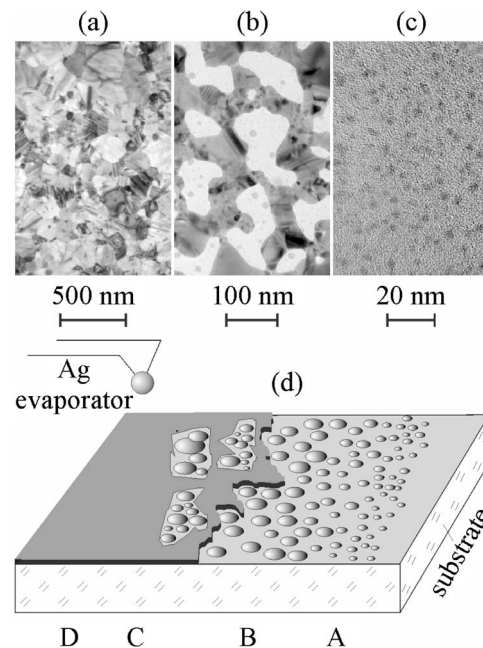


FIG. 2. Upper part: TEM images of Ag films on 10 nm carbon foil with mass thicknesses of (a) 33, (b) 2.5, and (c) 0.6 nm. Lower part: (d) schematic view of the film, defining areas A (isolated clusters of a few nanometer size), B (isolated clusters with a size up to several tens of nanometers), C (percolated film with nanoparticles in gaps), and D (closed film).

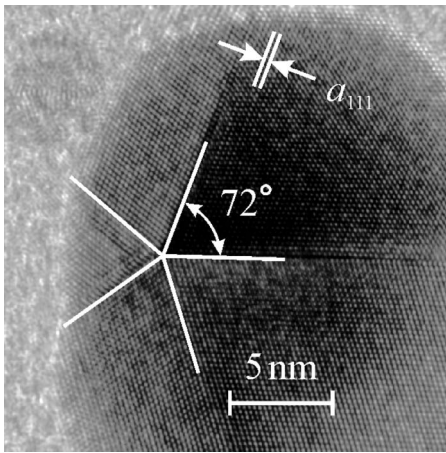


FIG. 3. HRTEM image of Ag particles located in a gap between continuous islands of the Ag film with a mass thickness of 2.5 nm: decahedral particle with 20 nm diameter with resolved fringes of atomic planes of (111) orientation and icosahedral particle with 5 nm diameter in the upper left corner.

probe pulses, and one path was temporally delayed with respect to the other by a computer-controlled optical delay stage. Before being directed into the UHV device, both beams are collinearly combined by a second beam splitter.

### III. SAMPLE CHARACTERIZATION

The structures of the Ag films obtained by means of HRTEM are shown in Figs. 2(a)–2(c) (upper part). As can be seen from (a), the Ag film with a mass thickness of 33 nm is polycrystalline and continuous (i.e., closed). With decrease in the mass thickness, gaps appear in the continuous film. Further decrease in the mass thickness leads to an increase in the gaps so that within the gaps, separate Ag particles are observed on the bare substrate. At a mass thickness of 2.5 nm, the typical lateral size of these particles in the gaps is 10 nm (b). The Ag film with smaller mass thickness consists of isolated particles in the few nanometer size range only (c).

Along with HRTEM characterizing the lateral dimensions, AFM was used for precise measurements of the structure of different regions of the Ag film in the direction perpendicular to the substrate. In combination, both methods determine their mass thickness  $d_{\text{eff}}$ .

The lower part in Fig. 2 shows the schematic view of the film with a wedge-shaped thickness. With increasing mass thickness, we find isolated small clusters of a few nanometer size (region A), clusters with gradually growing size up to several tens of nanometers (region B), clusters that partly coalesced (region C), and finally, a closed Ag film (region D).

Structural investigations allowed us not only to characterize the different areas of the wedge-shaped Ag film (coefficient of the substrate coating, particles' average sizes, and distances between them), but also provide additional information about the work function  $\phi$  of particles with different sizes. Following the Fowler equation for the thermionic

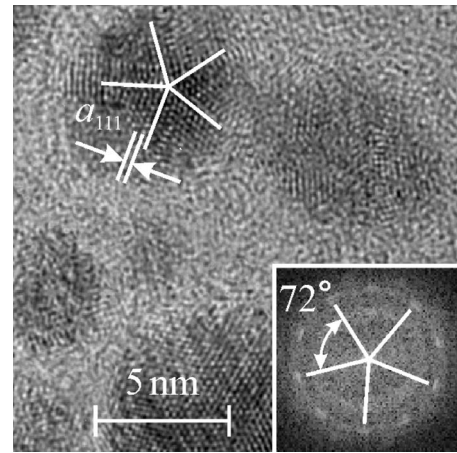


FIG. 4. HRTEM image of the Ag particle film with a mass thickness of 0.6 nm. The Fourier transform of the image of the decahedral particle in the upper left corner is given in the inset. It contains ten reflexes of the 111 type illustrating the fivefold symmetry of the multiple-twinned particle.

emission and the Fowler–DuBridge–Bechtel equation for the thermally assisted photoemission,<sup>5</sup> the total photoemission yield critically depends on  $\phi$ . Therefore, the particle-size dependence of  $\phi$  has to be taken into account for a correct interpretation of our experimental data. Figure 3 is a high-resolution TEM image of a single Ag nanoparticle with a size (diameter)  $a=20$  nm in a gap of the Ag film as shown in Fig. 2(b), providing insight into the structural details. Particles of this kind are visible as faint dark spots in the bright areas of Fig. 2(b). The particle analyzed in Fig. 3 is a decahedron characterized by a fivefold symmetry axis normal to the image plane passing through the point in which the twinned boundaries converge (they are marked with white lines). In the image of this particle, the atomic planes of (111) orientation being parallel to the twinned boundaries are visualized. The distance between them is  $a_{111}=0.2361$  nm. The smaller the particle size, the more essential are surface effects. The minimum of the particle free energy is achieved for the minimum surface energy. The multiple twinned particles (decahedron, icosahedron) satisfy these requirements (the shape of such particles approaches the ideal spherical shape, and they are formed from facets with the smallest surface energy). Their formation is typical in the case of a weak interaction with the substrate. Faceting of the multiple twinned particles determines their work function. It is known that the electronic work functions are 4.5, 4.6–4.7, and 4.9 eV for facets of a clean Ag monocrystal of (110), (100), and (111) orientations, respectively.<sup>6–8</sup> Hence, we conclude that the work function of relatively large Ag particles like that in Fig. 3 (decahedron with a lateral size  $a$  of about 20 nm) is close to 4.9 eV, as long as the surface is clean and screening effects by the substrate can be neglected.

Another dodecahedral particle with a size (diameter) of 5 nm is shown in the upper left corner of Fig. 4 (mass thickness of 0.6 nm). Its diffraction pattern (Fourier transform) shown in the inset in Fig. 4 shows five pairs of (111)-type spots. This Ag particle is faceted by closely packed surfaces of the (111) type too, but due to the size dependence of the

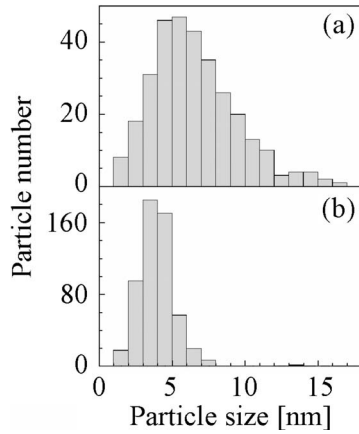


FIG. 5. Histograms of particle-size distributions for Ag films with mass thicknesses of (a) 1.2 nm and (b) 0.6 nm.

work function, the latter is smaller than 4.9 eV. It is known that the size dependence of the work function is non-monotonic<sup>9–12</sup> (see also Refs. 13 and 14). For metal particles with sizes falling within the range  $15 \text{ nm} > a > 2\text{--}3 \text{ nm}$ , the work function decreases due to an increase in the contribution from weakly coordinated atoms, which belong to the surface. (The electron work function is identified with the averaged orbital electronegativity of the surface atoms. It can be presented as a function of the number of broken links.) For even smaller particles ( $a < 2\text{--}3 \text{ nm}$ ) the work function grows due to the dominating contribution of the image forces and finally of the quantum-size effect.

Ag films with a mass thickness of  $d_{\text{eff}} < 1.5\text{--}2 \text{ nm}$  contain only insulated nanoparticles, percolation is not observed here. Histograms of the particle size distribution for Ag films with mass thicknesses of  $d_{\text{eff}} = 1.2$  and  $0.6 \text{ nm}$  are shown in Figs. 5(a) and 5(b), respectively. The clusters were assumed to have a spherical shape.

We recognize that the  $0.6 \text{ nm}$  distribution (b) is rather narrow, centering at a size (diameter) of  $4 \text{ nm}$  with a FWHM of about  $2.5 \text{ nm}$  only. There are no particles with sizes (diameters)  $> 8 \text{ nm}$ . The  $1.2 \text{ nm}$  distribution (a) centers only slightly higher (at  $5.5 \text{ nm}$  diameter) but is much wider (about  $6.5 \text{ nm}$  FWHM) and extends up to diameters of  $15 \text{ nm}$ . This result is important in the context of size-selective excitations, see below.

#### IV. RESULTS

##### A. Dependence of the electron yield on the Ag mass thickness

The experimental dependences of the electron emission current versus mass thickness for excitation with the  $800 \text{ nm}$  (a) and  $400 \text{ nm}$  (b) laser beams are given in Fig. 6. The distance from the thick edge of the wedge-shaped Ag film and its mass thickness are plotted on the abscissa at the bottom and at the top, respectively. For the measurement, the average powers of the infrared and blue laser beams differed and were equal to  $600$  and  $100 \text{ mW}$ , corresponding to fluences of  $80$  and  $16 \mu\text{J}/\text{cm}^2$  per pulse at pulse durations of  $18$  and  $27 \text{ fs}$ , respectively. Due to these short pulse lengths, the photon energy bandwidths are rather large, i.e.,  $1.55 \pm 0.07$  and

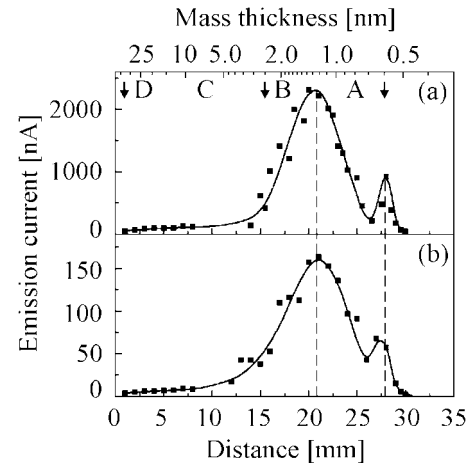


FIG. 6. Electron emission current from a Ag film with wedge-shaped thickness profile. The distance from the edge of the film and corresponding mass thickness are plotted on the bottom and top abscissa, respectively. The results correspond to laser excitation at (a)  $800 \text{ nm}$ ,  $500 \text{ mW}$ ,  $18 \text{ fs}$  pulses and (b)  $400 \text{ nm}$ ,  $100 \text{ mW}$ ,  $27 \text{ fs}$  pulses. The curves through the experimental points are to guide the eye. Regions A–D correspond to the TEM images in accordance with Fig. 2, lower part.

$3.1 \pm 0.15 \text{ eV}$ , respectively. The latter interval covers the central range of the particle plasmon resonance spectrum of Ag. The maximum thicknesses of the studied Ag films was  $33 \text{ nm}$ . The penetration depth  $d^*$  of the  $800$ ,  $400$ , and  $250 \text{ nm}$  radiations are about  $10$ ,  $15$ , and  $16 \text{ nm}$ , respectively. This makes it possible to measure the photoemission current of the Ag film in the transmission mode, i.e., from the direction opposite to its illumination.

In region D, the laser-induced signal is very small for both wavelengths, cf. Fig. 6. This means that multiphoton photoemission from the closed Ag film or from extended Ag islands is negligible on the intensity scale of Fig. 6. Note that our geometry corresponds to *s*-polarized excitation that is “parity unfavored” because the electric vector lies parallel to the surface. This leads to preferential electron excitation in the surface plane, whereas we detect the electrons above the surface. In addition, the transparency is only a few percentage for  $33 \text{ nm}$  Ag film thickness at the  $800 \text{ nm}$  radiation.

In region C, the decrease in the mass thickness is accompanied by the appearance of gaps in the continuous film, i.e., the coating coefficient decreases. In this range, the multiphoton photoemission signal of electrons increases due to an increase in the film roughness.<sup>15</sup> The formation of gaps in the continuous film comes along with an increase in its roughness. The gradual increase of the photoemission intensity with decreasing mass thickness  $d_{\text{eff}}$  in region C (between  $5$  and about  $2.5 \text{ nm}$ ) very likely results from this effect, see Fig. 6.

In the region where Ag particles on the  $10 \text{ nm}$  size scale are found inside the gaps of the Ag film, the photoemission current abruptly increases (boundary of regions C and B at about  $3 \text{ nm}$ ). This increase amounts to 1 and 2 orders of magnitude at  $\lambda = 400$  and  $800 \text{ nm}$ , respectively. This result is most probably determined by a mechanism of photoelectron emission, which is femtosecond-laser-induced thermionic

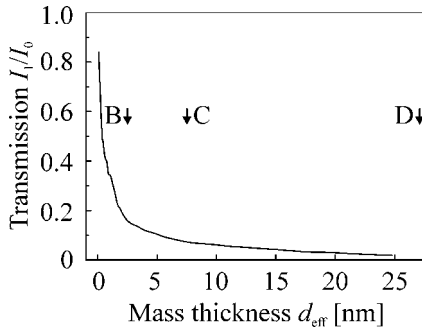


FIG. 7. Measured transmission of the wedge-shaped Ag film for the 800 nm laser beam with an average power of 590 mW. The same designations as in Figs. 2 and 6 are used.

emission from nanoparticles, which competes with the “conventional” multiphoton photoemission studied in bulk materials.<sup>1</sup> The origin of this process will be discussed in detail below. It agrees with prior experiments,<sup>4</sup> in which it has been demonstrated that upon excitation at 400 nm, the transition from a continuous film to a nanoparticle film is characterized by a strongly increasing electron yield and, more essential, by a change in the electron energy distribution.

Although resonant absorption by coupling of the exciting light to localized plasmon modes of the particles is certainly present and leads to an enhancement in the electron yield,<sup>16</sup> this process does not determine the shape of the curves in Fig. 6. The characteristic plasmon resonance energies of Ag particles are located around 3 eV, i.e., it is relevant for the 400 nm excitation. Much lower energies may be possible in the case wherein the particle exhibits extreme deviations from a spherical shape. The measured dependence of the transmission for the infrared laser beam on the mass thickness of the Ag film is shown in Fig. 7. As can be seen, the curve is essentially unstructured, thus ruling out significant resonance features for certain particle sizes. For relatively wide size distributions like in Fig. 5(a), we expect that certain particles are resonantly excited (see next section) but this does not lead to significant features in the yield spectra in Fig. 6 because the experiment averages over the size fractions of the selected microarea of interest.

Figure 6 reveals that under illumination at 400 and 800 nm, the dependence of the photocurrent on the mass thickness of the Ag film exhibits qualitatively the same behavior. Obviously, this reflects the structural properties of the film in different regions. With decreasing mass thickness in region C, the emission current slowly increases. In the range of  $d_{\text{eff}} < 2.5$  nm, the current steeply increases and exhibits two maxima at about 1.2 and 0.6 nm mass thicknesses. The current for  $d_{\text{eff}} = 1.2$  nm (first maximum) exceeds the current for  $d_{\text{eff}} = 33$  nm by almost 2 orders of magnitude and by more than 1 order of magnitude for 800 and 400 nm excitations, respectively. We presume that the second maximum at  $d_{\text{eff}} = 0.6$  nm is related to a change in the emission mechanism, as will be discussed below (see Sec. V).

The continuous film D, the percolated island film with gaps C, the region with larger particles B, and the region A with smaller particles adjacent to B have a sufficiently high

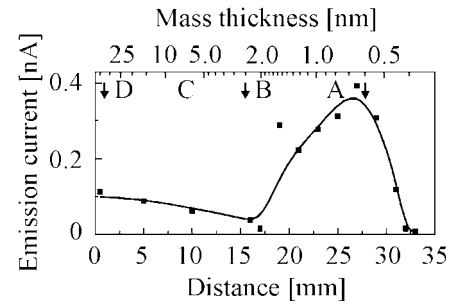


FIG. 8. Electron emission current from the same film as Fig. 6 but under a high-pressure Hg lamp excitation ( $h\nu \leq 5.2$  eV). The same designations as in Figs. 2, 6, and 7 are used.

conductivity to avoid charging of the sample. Here, the particle film is an ensemble of Ag particles coupled by tunneling through the glass substrate.<sup>12</sup> However, upon further decrease in the mass thickness, the Ag particle film is characterized by a decrease in the particle size as well as by an increase in the average distance between them. The latter causes loss of the tunneling conductivity. Hence, Ag films with a mass thickness of  $d_{\text{eff}} < 0.4$  nm could not be studied in the present work because of their insufficient electrical conductivity that resulted in charging of the sample during the photoemission measurements.

For comparison, an identical film has been investigated under illumination with the high-pressure Hg lamp, i.e., for the case that the quantum energy exceeds the work function of electrons from Ag. This result shown in Fig. 8 reflects normal 1PPE or threshold emission, originating from the near-surface region with a depth of a few nanometers. In regions D and C, the decrease in the mass thickness leads to a decrease in the electron emission current for UV excitation reaching a minimum at about  $d_{\text{eff}} \approx 2.5$  nm. This behavior most likely just reflects the amount of material in the overlayer. Upon further decrease in the mass thickness, the photocurrent rapidly increases. In the range of  $d_{\text{eff}} < 2.5$  nm (regions B and A), the dependence of photoemission current on mass thickness exhibits a nonmonotonous behavior with a maximum at 0.6–0.7 nm. Obviously, the cluster film has a higher photoemission yield compared to the closed film in regions D and C. For the continuous film in these regions, threshold photoemission is possible if an electron has a total energy exceeding the vacuum level, and its momentum is directed within the so-called escape cone with respect to the surface normal.<sup>17</sup> This leads to a strong discrimination of all momentum vectors outside of this cone. The latter requirement is absent for the case of a nanoparticle film, thus allowing practically all electrons with sufficient energy to leave the particle. Furthermore, the 2 mm diameter UV beam causes a considerable photoconductivity of the surface. This shifts the emission cutoff to lower mass thicknesses ( $\approx 0.4$  nm) as compared to the results for laser excitation shown in Fig. 6.

### B. Dependence of the electron yield on the laser power

To shed further light into the mechanism of electron emission, the dependence of its intensity on the power of the laser

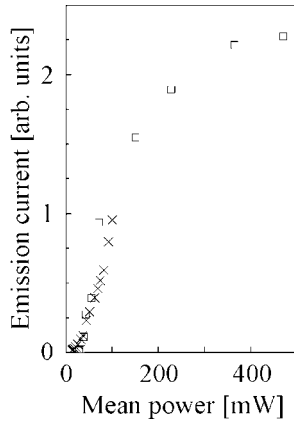


FIG. 9. Electron emission current versus average laser power for Ag particle film with mass thickness of 1.2 nm at 800 nm (squares) and 400 nm excitations (crosses).

beam is informative. In the case of  $n$ -photon photoemission ( $n$ PPE), it takes a power law with the integer exponent of  $n$ .<sup>18</sup> However, experiments by Schmidt and co-workers<sup>19,20</sup> clearly revealed deviations from integer exponents. The fractional exponent  $\alpha$  even varied across the field of view in the PEEM experiment. Figure 9 shows the dependence of the photoemission intensity of the Ag film with  $d_{\text{eff}}=1.2$  nm on the average power upon excitation with 800 nm (squares) and 400 nm (crosses) laser radiations. These curves were scaled to superimposed each other. The maximum of the particle-size (diameter) distribution histogram corresponds to about  $a=5$  nm [see Fig. 5(a)]. Under 400 nm excitation, the dependence of the photocurrent on the beam power exhibits the expected value of  $n=2$  within the experimental uncertainty of  $\pm 0.05$  (see Fig. 10). Obviously, this is a clear fingerprint of true 2PPE throughout the accessible power range from 15 to 100 mW.

In the case of 800 nm excitation, the accuracy of the measurements does not allow us to approximate the experimental curves with a power function. These measurements are interesting because they were performed in a wider laser power range (up to 500 mW). They show saturation at laser power densities above 300 mW that corresponds to a field strength value of  $E \sim 3 \times 10^6$  V/cm. The saturation most likely results from space charge effects.

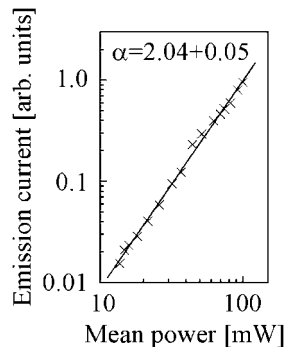


FIG. 10. Result on a log-log scale with linear fit of the measurement at 400 nm, shown in Fig. 9 (crosses).

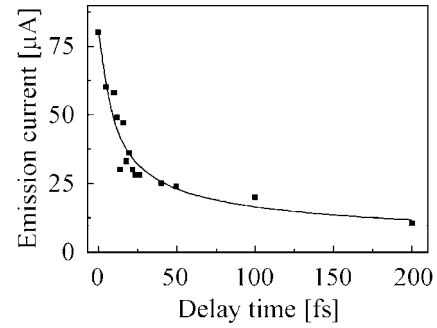


FIG. 11. Electron emission current measured for a Ag film with mass thickness of 1.2 nm versus delay time between pump-and-probe pulses (photon energy of 1.55 eV, pulse width of 30 fs, average power of both pump-and-probe beams of 100 mW). The full line serves to guide the eye, the dashed line denotes twice the current measured for the case that the probe or pump beam is blocked.

### C. Dependence on the pulse width and pump-probe measurements

The dependences of the electron yield on the pulse width of the laser and on the delay in a pump-probe setup are closely related. The result of the pump-probe experiment shown in Fig. 11 was obtained for a Ag film with  $d_{\text{eff}}=1.2$  nm using 800 nm excitation. These data give us information on the temporal correlation between two laser pulses incident on the sample. Any correlation time exceeding the temporal width of the laser pulses is characteristic for a sample-intrinsic response time to the laser-induced excitation. To exclude the optical field emission mechanism, the pump-and-probe beams were set to equal the average power of 100 mW and equal pulse widths of 30 fs. Note that this value is only 12 fs (60%) larger than the pulse width of the fundamental beam used for the studies of the electron emission on the mass thickness and the power dependences. Such a small broadening of the pulse width led to a decrease in the electron emission current from 2000 nA at 18 fs width down to 80 nA at 30 fs width [Figs. 6(a) and 11].

Upon the combined action of both pulses, the electron emission current strongly exceeds the sum of photoemission currents for the cases when either the pump beam or the probe beam is blocked. The shorter the delay time  $\Delta\tau$  between the pump-and-probe pulses, the more significant is this effect. The photoemission currents for the cases when only the pump beam or only the probe beam is active are about 5 nA, i.e., 10 nA in sum. Indeed, with the accuracy of the measurements for the combined action of the pump-and-probe beams, the current is equal to 10 nA for delay times  $\Delta\tau > 200$  fs, see Fig. 11. This delay is much larger than the pulse width of the pump-and-probe beams (30 fs) but much less than the distance between adjacent pulses, being  $\sim 12$  ns (at the repetition rate of the laser oscillator being 82 MHz). When switching on the second beam at  $\Delta\tau=0$ , the power is doubled but the current goes up by a factor of 16 (from 5 nA for one 100 mW beam to 80 nA for both beams, i.e., 200 mW). More important, we observe an increase in this time with decreasing mass thickness (i.e., decrease in the average particle size) up to values of several picoseconds.

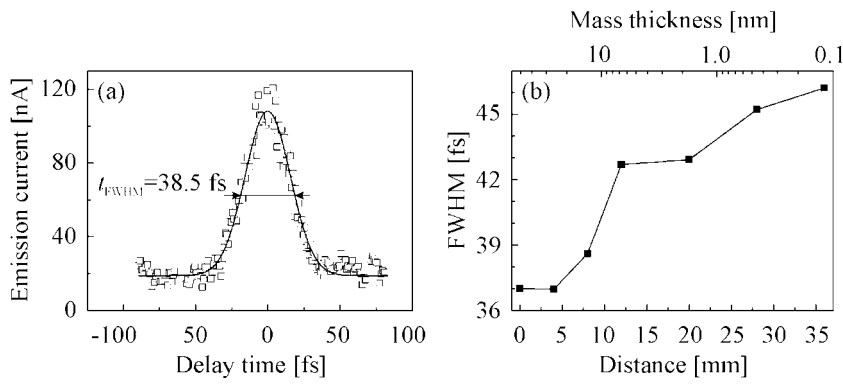


FIG. 12. (a) Autocorrelation trace as obtained during a monochromatic pump-probe experiment (quantum energy of 1.55 eV, pulse width of 30 fs) on a gold film. (b) Dependence of the FWHM of the autocorrelation trace on the distance of the gold film from the evaporator. The corresponding mass thickness is shown on the top.

We also studied the dependence of the electron emission intensity on the time delay between pump-and-probe pulses for a gold particle film. A typical autocorrelation trace is shown in Fig. 12(a). Its FWHM increases with decreasing mass thickness of the film [Fig. 12(b)]. It shows that the microscopic mechanism responsible for the photoemission is strongly affected by the size of the particles. This confirms the result of a quantum-statistical treatment<sup>21</sup> that the probability of thermionic and thermally assisted multiphoton photoemission increases when the particle size decreases. The steplike increase in the relaxation time at a mass thickness of 10 nm is most likely attributed to the appearance of gaps in the gold film and clusters emerging inside the gaps.

Besides, there is the quantization of energy levels in the conduction band, and the distance between levels increases with decreasing size. Thus, if a nanoparticle is small enough, the quantization of energy levels should manifest itself in a greater relaxation time because the laws of conservation of energy and pulse should be met in the case of electron-electron scattering. It is obvious that it is difficult to achieve when some values of energy and pulse are forbidden.

In a similar way, the dependence of the electron emission intensity on the laser pulse width is informative for understanding the mechanism of electron emission. The minimum laser pulse width used in this setup was 85 fs and the average power was 400 mW. The current sensitivity of the detection was 0.1 nA.

Figure 13 illustrates this dependence for excitation at 800 nm and for Ag films with three different mass thicknesses of  $d_{\text{eff}}=0.6$  (curve 1), 1.2 (curve 2), and 2.5 nm (curve 3), respectively. This measurement can be considered as a quasi-pump-probe experiment where only one wing of the autocorrelation trace is measured. The maximum emission current registered in this experiment was 30 nA, which is 2 orders of magnitude smaller than the current from the same sample excited by 18 fs pulses, see Fig. 6. Due to the increase in the peak intensity, a decrease in the laser pulse width at a fixed average power causes an increase in the electron emission intensity. This effect is nonlinear and depends again on the particle size. The nonlinear slope of this dependence becomes weaker when the Ag particles become smaller: curves 1 and 2 correspond to average particle sizes (diameters) of  $a=3.5$  and 5 nm, curve 3 is measured on an island film with gaps.

This behavior cannot be understood by assuming a common multiphoton photoemission. In the framework of ther-

mally assisted multiphoton photoemission,<sup>5</sup> this means that the electron and phonon subsystems remain in the nonequilibrium state longer in the case of smaller particles. This experimental result agrees with the suggestion of a reduced electron-phonon coupling in small particles.<sup>22</sup> The photoemission current dropped below the sensitivity limit of 0.1 nA of the used picoampere meter for films with mass thicknesses  $d_{\text{eff}} \geq 3$  nm.

## V. DISCUSSION

The above results indicate a change from the multiphoton photoelectron emission process dominating for a continuous Ag film to another prevailing mechanism acting in the case of a particle film for excitation with the femtosecond laser. The electron emission current first increases with decreasing mass thickness because of an increasing number of clusters in the film. Below  $d_{\text{eff}}=1.2$  nm, the current decreases because the amount of Ag drops and tends to zero. It means that the nonmonotonous dependence of the photoelectron emission current on the mass thickness of the Ag film in the range of  $d_{\text{eff}} < 2.5$  nm is not directly related to the emission mechanism. This conclusion follows from the fact that the positions of the main maxima of these curves for the two wavelengths coincide [left dashed line in Fig. 6] while the emission mechanisms are different. The maximum at 1.2 nm simply reflects an “optimum” particle density in the film, i.e., it is a structural feature of the film morphology. In the right boundary of region A where multiphoton photoemission is

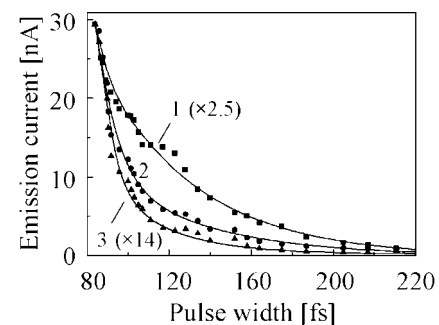


FIG. 13. Electron emission current measured as a function of the width of the laser pulse for Ag cluster films with mass thicknesses  $d_{\text{eff}}=0.6$  (curve 1), 1.2 (curve 2), and 2.5 nm (curve 3) excited at 800 nm (average power kept fixed at 400 mW).

weakened due to the reduced amount of metal (right dashed line in Fig. 6), the increasing number of particles with size (diameter)  $<5$  nm most likely gives rise to the thermally assisted electron emission channel, which is present at both photon energies as predicted by the statistical model in Ref. 21.

Striking characteristics of this emission process are the rather moderate dependence of the electron yield on the excitation wavelength and the specific and particle-size dependent temporal response (see Figs. 9–13). As discussed above, both effects cannot be brought in line with a conventional multiphoton photoemission process. Instead, we can relate the electron emission at least partly to a laser heating of the electron gas in the metal particles. This emission channel opens if sufficient energy can be fed into and accumulated in the electron subsystem of the particle. Fast and efficient concentration of electromagnetic energy into the small particles is facilitated by the high peak power of the short laser pulses, in particular, for the fundamental of the Ti:sapphire laser at 800 nm. The 18 fs pulses have a peak power of  $4 \times 10^5$  W. The peak power of the 400 nm pulses is lower due to the frequency conversion and longer duration of 27 fs pulse, resulting in  $4 \times 10^4$  W. However, the optical response of the particles at 400 nm is enhanced due to the vicinity of the surface plasmon polariton of Ag that can substantially enhance extinction and absorption cross section.<sup>23</sup> Nevertheless, the electron yield for the infrared pulses is more than 1 order of magnitude higher, cf. Fig. 6. The heating of the electron gas by the laser pulse initially leads to a strongly non-Fermi–Dirac distribution<sup>24</sup> and later results in a Fermi–Dirac-type distribution with a high-energy tail and more electrons can then participate in the *n*PPE process. In this connection, it is helpful to remind that on the subpicosecond time scale, the electron and phonon gas are initially decoupled, where the efficiency of the internal energy transfer between both subsystems is determined by the electron-phonon coupling constant.

Consequently, heating of the electron gas with a femtosecond-laser pulse gives rise to a transient nonequilibrium ( $T_e > T_{ph}$ ) state. At temperatures  $T_e$  high enough (by analogy with the thermionic emission, it is  $\geq 2000$  K), the tail of the non-Fermi–Dirac electron energy distribution exceeds the vacuum level. Electrons from this tail area can leave the cluster and escape into the vacuum. Due to multiple scattering processes, these electrons have lost their “memory” on the initial photoexcitation, comparable to the so-called true secondaries that arise in any photoemission experiment with sufficient excess energy. The total emission current  $j$  is given by the Richardson–Dushman equation for thermionic emission.<sup>25,26</sup> This equation contains no explicit dependence on the excitation wavelength. Implicitly, however, the achievable electron gas temperature  $T_e$  is in first order governed by the absorbed fluence of the incident electromagnetic wave and depends, therefore, on the wavelength-dependent absorption cross section of the material. In the visible regime, this dependence is rather weak and the sensitivity of the total photoemission yield on the photon energy should be much less pronounced than in the case of multiphoton photoemission, in correspondence with our experimental observations.

To account for the observed particle-size dependence of the photoemission yield characteristics (see Figs. 6, 8, and 13), the exponential dependence on  $T_e$  and the work function comes into play. For a metal, we can estimate the mean free path  $l_{e-ph}$  for electrons close to  $\varepsilon_F$  by  $l_{e-ph} = \tau \cdot v_F$ , where  $\tau$  is the Drude relaxation time and  $v_F$  is the Fermi velocity. For silver at room temperature, the values of  $\tau$  and  $v_F$  are 40 fs and  $1.4 \times 10^8$  cm/s,<sup>27</sup> giving rise to 60 nm mean free path, which is indeed much larger than the size (diameter)  $a$  of the particles under investigation. The inequality  $a < l_{e-ph}$  means that the electron in the particle can move without phonon scattering, reflecting several times from its surface, comparable to an electron oscillator. For evaluation of its frequency  $\omega_e = v/a$ , let us assume the Fermi velocity for Ag  $v_F$  (see above) and a particle size of  $a = 10$  nm. Thus, the frequency of the electron oscillator  $\omega_e = 10^{14}$  s<sup>-1</sup> significantly exceeds the Debye frequency (maximum frequency of the phonon spectrum) for Ag  $\omega_D = 4.7 \times 10^{12}$  s<sup>-1</sup>.<sup>28</sup> The smaller the particle size, the stronger is the inequality  $\omega_e \gg \omega_D$  and, therefore, the weaker is the interaction between the electron and phonon subsystems. Weakening of the electron-phonon interaction means that the energy absorbed by the particle from the laser pulse is more efficiently stored by the electron subsystem before being transferred to the phonon system, so that the electron gas dwells at high temperatures for a longer time. Such a weakening in the electron gas cooling rate for small particles fits to the observed dependence of the photoemission current on the laser pulse width and, hence, laser pulse intensity (Fig. 13) which becomes less steep as the particles become smaller. For the different laser pulse widths, the changes in  $T_e$  and, therefore, the changes in the emission yield are obviously less pronounced for small particles than for the larger ones. Such an observation does not follow from the mechanism of the instantaneous multiphoton photoemission.

The role of the work function of the silver particles with respect to the dependence of the photoemission yield on particle size as shown in Fig. 6 was already discussed in Sec. III. The exponential dependence of the thermionic emission current on  $\phi$  in the Richardson–Dushman equation accounts for the appearance of the work function governed maximum in the photoemission yield located at  $d_{eff} = 0.6$  nm in the case of excitation of the particles with the pulsed lasers.

The threshold photoemission under excitation with the UV lamp is also determined by the work function. Thus, the position of the maximum of the curve in Fig. 8 reflects the minimum of the work function of the particles followed by the steep drop at  $d_{eff} = 0.5$  nm caused by the increase in the work function for very small particles along with the low conductance of the cluster layer at low coverage.

An especially eye-catching result is the power dependence of the electron yield, see Fig. 9. What do we expect in femtosecond-laser-induced thermionic emission when the energy pumped in the particle is successively increased? Initially,  $T_e$  will increase, however, this increase is limited by the fact that with growth of the electron temperature, the heat capacity of the electron subsystem also increases.<sup>22</sup> The electron temperature grows until a balance between the amounts of energy fed to the electron subsystem from the outside and transferred from it to the phonon subsystem is achieved. It

means that the value of the electron temperature and, therefore, the electron emission intensity tend to saturation with growth of input power. Nonlinear dependence of power transferred from the electrons to the phonons,  $\sim(T_e^2 + T_{ph}^2)$ , as well as the fact that with growth of the electron temperature additional ways of energy dissipation from the electron gas can appear, promotes the saturation. The data points for the 800 nm excitation in Fig. 9 (squares) show the same saturation. Thus, the saturation in Fig. 9 does not contradict this mechanism. It is absent for the data points for the 400 nm excitation beam because the maximum value of the average power of the 400 nm laser beam is a factor of 5 smaller than that of the 800 nm laser beam.

The saturation can also be explained by using the Rethfeld formalism. Following Ref. 24, after a low-power excitation, the phonon cooling of the nonequilibrium electron gas is much less efficient than the cooling of a corresponding thermalized Fermi-distributed electron gas, while in the case of a strong perturbation, the cooling of the laser-excited electron gas by phonon emission is nearly as efficient as the cooling of the Fermi-distributed electron gas. Therefore, the cooling rates of the electron subsystem are far from being the same for low- and high-power excitations.<sup>24</sup> This means that in the case of low-power excitation, the electron subsystem stays thermally decoupled from the phonon bath for a longer time, favoring the thermionic emission mechanism.

Let us estimate the quantum yield of electron emission. As is seen from Fig. 6, the maximum of the photocurrent is observed for excitation of the particle film with  $d_{eff} = 1.2$  nm by using the femtosecond-laser system. This corresponds to an emission current of  $I_e = 2.3 \mu A$  for the infrared laser beam with an average power of  $P = 500$  mW and to  $I_e = 0.16 \mu A$  for the blue laser beam with an average power of 100 mW. Thus, the quantum yields are  $(I_e/e)/(eP/h\nu) \approx 7 \times 10^{-6}$  and  $5 \times 10^{-6}$  electrons per infrared and blue photons, respectively. It should be noted that good scintillators are characterized by a quantum yield of  $10^{-8}$ . An increase in the quantum yield of photoelectrons from metal nanoparticles is described in Refs. 29–31. The quantum yield increases further by several orders of magnitude if a Ag particle film is activated by cesium and oxygen.<sup>32,33</sup>

Now, we will estimate what maximum values the electron temperature can reach in the present experiment. The duration of the femtosecond-laser pulses was varied from tens to hundreds of femtoseconds, i.e., it lies between the characteristic times of the electron-electron  $\tau_{e-e} = 1-10$  fs (Refs. 34 and 35) and electron-phonon  $\tau_{e-ph} = 1$  ps (Refs. 36–38) interactions. The thermalization times of the electron and phonon subsystems is less than 1 ps (Refs. 24 and 39) and 1–10 ps (Refs. 24, 35, and 39–41), respectively. Thus, the heat transfer from the electron subsystem to the phonon system can be neglected during the action of our short laser pulses. Therefore, the change in the electron gas temperature  $dT_e$  and increment in the thermal energy  $\delta Q$  (from the laser pulse) are related by the expression

$$\delta Q = C_e dT_e. \quad (1)$$

The heat capacity of the electron gas depends on its temperature, and for  $N$  electrons takes the following form<sup>42</sup>:

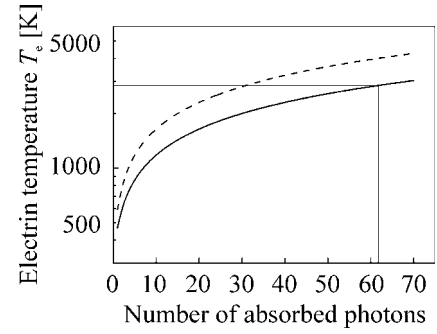


FIG. 14. Maximum electron temperature  $T_e$  (in the sudden approximation) induced in a spherical Ag particle (diameter of 5 nm) as a function of the number of absorbed photons. The curves refer to absorption of 1.55 eV (full line) or 3.1 eV photons (dashed line). In the case of 100% absorption of an infrared laser single pulse with fluence of  $8 \times 10^{-5}$  J/cm<sup>2</sup>, corresponding to 63 photons per 5 nm diameter particle (vertical line), the electron temperature would reach 3000 K.

$$c_e = \frac{\pi^2 k_B^2}{2\varepsilon_F} T_e N = \gamma T_e N, \quad (2)$$

where  $\gamma = \pi^2 k_B^2 / 2\varepsilon_F = 6.2 \times 10^{-9}$  eV/K<sup>2</sup>. We will integrate expression (1) and derive  $T_e$  from it. Thus, by neglecting all kinds of energy dissipation (“sudden approximation”), we have the following for the transient electron temperature:

$$T_e = \sqrt{\frac{2Q}{\gamma N} + T_{ph}^2} = \sqrt{3.2 \times 10^8 \frac{Q}{N} + T_{ph}^2}. \quad (3)$$

The fluence in a single pulse of the 800 nm laser beam with an average power of 500 mW and diameter of 100  $\mu m$  is  $J = 8 \times 10^{-5}$  J/cm<sup>2</sup> =  $5 \times 10^{14}$  eV/cm<sup>2</sup>. We assume a Ag particle size of  $a = 5$  nm [according to Fig. 6(a) corresponding to a Ag film with  $d_{eff} = 1.2$  nm, for which the maximal electron emission is observed] and a density of Ag atoms of  $\rho = 5.9 \times 10^{22}$  cm<sup>-3</sup>. Then, we arrive at 63 photons per 5 nm particle so that per electron fall on average  $3J/2a\rho = 0.025$  eV for the 800 nm laser pulse. Substituting  $Q/N = 0.025$  eV and  $T_{ph} = 300$  K (room temperature) in expression (3) gives 2800 K. The density of electron states in Ag as well as reflection, transmission, and local statistical fluctuations in the photon flux density were not taken into account in this estimation. In fact, the quantity of energy absorbed by an individual particle can deviate strongly from the average value.<sup>21</sup> The latter statistical effect is the more essential, the smaller the particle size.

The derived dependence in Eq. (3) is plotted in Fig. 14 for the infrared and blue laser beams. It can be clearly seen that the contribution of the hot electrons to the electron emission from a 5 nm particle cannot be neglected even if only 15% of the laser flux is absorbed. In this case, the maximal electron temperature is far beyond 1000 K. Also, it should be noted that the photoabsorption cross section of the metal particles can significantly exceed their geometrical cross section (criterion is the extinction coefficient of the particles at the given photon wavelength)<sup>43</sup> (see also Ref. 23). It depends on the size of the particles (proportional to the surface area,

i.e.,  $\sim a^2$ ), their shape, and the optical constants. As was shown above, in the present experiment, the Ag particles' shape was close to spherical (multiple twinned particles). In the general case, the absorption cross section significantly depends on the actual shape of the particles. This dependence is the more essential, the higher the value  $(\omega_p/\omega)^4$ , where  $\omega_p$  is the plasma frequency.

The energy distribution of photoexcited free electrons is deformed (non-Fermi-Dirac) and develops into a Fermi-Dirac distribution, which is described as transient electron gas heating after a certain time. When the temperature increase in the electron subsystem is small (low-perturbation regime), the tail of the thermal distribution of electrons does not reach the vacuum level. In this case, photoemission may appear due to the absorption of an additional photon by the heated electrons. However, sufficiently strong heating may lead to direct thermionic emission without absorption of a further photon. The higher the absorbed power and the lower the energy dissipation to the phonon subsystem, the higher the maximal electron gas temperature. The first condition can be realized by increasing the laser pulse power or decreasing the spot size or the pulse width and the second one can be realized by the reduction in the size of the metal particles. Au particles with sizes of a few tens of nanometers and smaller are stable to the irradiation with a CO<sub>2</sub> laser with a power density of 0.1 J/cm<sup>2</sup> (wavelength of 10.6 μm, pulse width of 1 μs).<sup>44–46</sup> This is 4 orders of magnitude higher than in the present paper. Thus, in the case of infrared illumination ( $h\nu=0.1$  eV) where the multiphoton processes are excluded, the escape of the electrons from the tail of their thermal distribution above the vacuum level is most likely responsible for the electron emission from Au nanoparticles. However, it is important to mention that (i) this long pulse width can be considered as cw excitation rather than pulsed excitation on the time scale of electron-phonon thermalization and (ii) the optical field emission mechanism<sup>47</sup> can also come into play at such low frequencies and high electromagnetic fields.

## VI. SUMMARY

In the present paper, we presented results of electron emission from Ag and Au films on a glass substrate with a gradient of the mass thickness from 0.1 to 40 nm under femtosecond-laser excitation at  $h\nu=1.55$  eV (pulse width of 18–300 fs, fluence of 80 μJ/cm<sup>2</sup>, photon flux of 3.3 nm<sup>-2</sup>) and at  $h\nu=3.1$  eV (pulse width of 27 fs, fluence of 16 μJ/cm<sup>2</sup>, photon flux of 0.32 nm<sup>-2</sup>), and also under UV excitation ( $h\nu\leq 5.1$  eV). In both cases, the photon energy

lies below the work-function threshold, thus excluding common single-photon photoemission. The main characteristics of the electron emission signal were presented, such as the dependence of the emission current on the pulse duration, the average power of the laser radiation, and the delay time in a pump-probe measurement. The results obtained allow to distinguish possible mechanisms of electron emission by means of analyzing a set of conditions of their realization. In particular, the following results were obtained:

(i) A strong increase in the electron emission intensity during transition from a continuous film to a particle film is observed under femtosecond-laser excitation with the quantum energy below the work function ( $h\nu < \phi$ ), which is in agreement with our previous measurements.<sup>4</sup> A corresponding increase, although weaker, was observed under excitation with a high-pressure Hg lamp ( $h\nu \geq \phi$ , i.e., threshold photoemission). We attribute this to the fact that the enhancement is partly a result of the structural properties of the films, i.e., an easier escape of the photoelectrons from particles with sizes in the few nanometer range as compared with a closed film along to a reduction in the work function in the cluster film.

(ii) In the whole range of mass thicknesses of the Ag particle film, the electron emission intensity upon excitation by the 800 nm laser beam (pulse width of 18 fs) is higher than that for the 400 nm laser beam (pulse width of 27 fs) despite the fact the 3PPE cross section is expected to be much lower than the 2PPE cross section. The average powers in both cases were of the same order of magnitude (a few hundreds of megawatts).

(iii) The photoemission intensity increases with decreasing pulse width in the range of 18–200 fs, but this dependence becomes less steep as the particles become smaller. This does not directly follow from an assumed mechanism of multiphoton photoemission.

(iv) Under excitation of the particle film by the femtosecond-laser, a more intense electron emission (by more than 2 orders of magnitude higher) obviously having a different mechanism is added to the pure multiphoton emission, which occurs for the continuous and percolated Ag films. It dominates for the particle films, in particular, for diameters below 5 nm. By comparison with model calculations and quantitative estimations, we could demonstrate that the additional mechanism is thermally assisted single—or multiphoton photoemission from a transient hot electron gas. This hypothesis is suitable to explain the whole set of the obtained experimental results.

\*FAX: 49-6131-3925412; nepijko@uni-mainz.de

<sup>1</sup>M. Bauer and M. Aeschlimann, *J. Electron Spectrosc. Relat. Phenom.* **124**, 225 (2002).

<sup>2</sup>W. Pfeiffer, C. Kennerknecht, and M. Merschdorf, *Appl. Phys. A: Mater. Sci. Process.* **78**, 1011 (2004).

<sup>3</sup>A. Kubo, K. Onda, H. Petek, Z. Sun, Y. S. Jung, and H. K. Kim, *Nano Lett.* **5**, 1123 (2005).

<sup>4</sup>M. Cinchetti, D. A. Valdaitsev, A. Gloskovskii, A. Oelsner, S. A. Nepijko, and G. Schönhense, *J. Electron Spectrosc. Relat. Phenom.* **137-140**, 249 (2004).

- <sup>5</sup>J. H. Bechtel, W. L. Smith, and N. Bloembergen, *Phys. Rev. B* **15**, 4557 (1977).
- <sup>6</sup>A. W. Dweydari and C. H. B. Mee, *Phys. Status Solidi A* **17**, 247 (1973).
- <sup>7</sup>A. W. Dweydari and C. H. B. Mee, *Phys. Status Solidi A* **27**, 223 (1975).
- <sup>8</sup>V. S. Fomenko and I. A. Podchernyaeva, *Emission and Adsorptive Properties of Substances and Materials, Handbook* (Atomizdat, Moscow, 1975).
- <sup>9</sup>R. Garron, *Ann. Phys. (N.Y.)* **10**, 595 (1965).
- <sup>10</sup>G. A. Katrich and A. G. Naumovets, in *Photoelectron Spectroscopy of Small Particles and Thin Films of s- and d-Metals: Size Effect in Their Electronic Structure*, Physics of Solid Surface, edited by J. Koukal (Elsevier, Amsterdam, 1987).
- <sup>11</sup>R. C. Baetzold, *J. Phys. (France)* **38**, C2-175 (1977).
- <sup>12</sup>R. D. Fedorovich, A. G. Naumovets, and P. M. Tomchuk, *Phys. Rep.* **328**, 73 (2000).
- <sup>13</sup>D. M. Wood, *Phys. Rev. Lett.* **46**, 749 (1981).
- <sup>14</sup>W. A. de Heer, *Rev. Mod. Phys.* **65**, 611 (1993).
- <sup>15</sup>J. T. Stuckless and M. Moskovits, *Phys. Rev. B* **40**, 9997 (1989).
- <sup>16</sup>G. P. Banfi, G. Ferrini, M. Peloi, and F. Parmigiani, *Phys. Rev. B* **67**, 035428 (2003).
- <sup>17</sup>G. K. L. Marx, H. J. Elmers, and G. Schönhense, *Phys. Rev. Lett.* **84**, 5888 (2000).
- <sup>18</sup>M. Aeschlimann, C. A. Schmuttenmaer, H. E. Elsayed-Ali, R. J. D. Miller, J. Cao, Y. Gao, and D. A. Mantell, *J. Chem. Phys.* **102**, 8606 (1995).
- <sup>19</sup>O. Schmidt, G. H. Fecher, Y. Hwu, and G. Schönhense, *Surf. Sci.* **482-485**, 687 (2001).
- <sup>20</sup>G. H. Fecher, O. Schmidt, Y. Hwu, and G. Schönhense, *J. Electron Spectrosc. Relat. Phenom.* **126**, 77 (2002).
- <sup>21</sup>A. Gloskovskii, Size-selective investigations of spectral and emission properties of small particles and nanotubes. Ph.D. thesis, University of Mainz, 2006.
- <sup>22</sup>P. M. Tomchuk, *Metallofiz. Noveishie Tekhnol.* **25**, 1233 (2003).
- <sup>23</sup>B. J. Messinger, K. U. von Raben, R. K. Chang, and P. W. Barber, *Phys. Rev. B* **24**, 649 (1981).
- <sup>24</sup>B. Rethfeld, A. Kaiser, M. Vicanek, and G. Simon, *Phys. Rev. B* **65**, 214303 (2002).
- <sup>25</sup>O. W. Richardson, *Philos. Mag.* **23**, 594 (1912).
- <sup>26</sup>S. Dushman, *Phys. Rev.* **21**, 623 (1923).
- <sup>27</sup>N. W. Ashcroft and N. D. Mermin, *Solid State Physics* (Saunders College Publishing, New York, 1976).
- <sup>28</sup>J. R. Neighbours and G. A. Alers, *Phys. Rev.* **111**, 707 (1958).
- <sup>29</sup>G. A. Katrich and O. G. Sarbei, *Sov. Phys. Solid State* **3**, 1181 (1961).
- <sup>30</sup>O. G. Sarbei and G. A. Katrich, *Ukr. Fiz. Zh. (Russian)* **6**, 418 (1961).
- <sup>31</sup>J. Lehmann, M. Merschorf, W. Pfeiffer, A. Thon, S. Voll, and G. Gerber, *Phys. Rev. Lett.* **85**, 2921 (2000).
- <sup>32</sup>F. Sabary and J. C. Dudek, *Vacuum* **41**, 476 (1990).
- <sup>33</sup>E. L. Nolle and M. Ya. Schelev, *Zh. Tekh. Fiz.* **30**, 1 (2004).
- <sup>34</sup>V. L. Ginzburg and V. P. Shabanskii, *Dokl. Akad. Nauk SSSR* **100**, 445 (1955).
- <sup>35</sup>R. H. M. Groeneveld, R. Sprik, and A. Lagendijk, *Phys. Rev. B* **51**, 11433 (1995).
- <sup>36</sup>J. G. Fujimoto, J. M. Liu, E. P. Ippen, and N. Bloembergen, *Phys. Rev. Lett.* **53**, 1837 (1984).
- <sup>37</sup>H. E. Elsayed-Ali, T. B. Norris, M. A. Pessot, and G. A. Mourou, *Phys. Rev. Lett.* **58**, 1212 (1987).
- <sup>38</sup>P. B. Allen, *Phys. Rev. Lett.* **59**, 1460 (1987).
- <sup>39</sup>S. I. Anisimov, Y. A. Imas, G. S. Romanov, and Y. V. Chodyko, *The Effect of High Power Radiation on Metals* (Nauka, Moscow, 1970).
- <sup>40</sup>N. Del Fatti, R. Bouffanais, F. Vallée, and C. Flytzanis, *Phys. Rev. Lett.* **81**, 922 (1998).
- <sup>41</sup>W. S. Fann, R. Storz, H. W. K. Tom, and J. Bokor, *Phys. Rev. B* **46**, 13592 (1992).
- <sup>42</sup>L. D. Landau and E. M. Lifshitz, *Statistical Physics: Course of Theoretical Physics* (Pergamon, Oxford, 1997), Vol. 5.
- <sup>43</sup>E. A. Manykin, P. P. Poluektov, and Yu. G. Rubezhnyi, *Sov. Phys. JETP* **43**, 1105 (1976).
- <sup>44</sup>L. I. Andreeva, A. A. Benditskii, L. V. Viduta, A. B. Granovskii, Yu. A. Kulyupin, M. A. Makedontsev, G. I. Rukman, B. M. Stepanov, R. D. Fedorovich, M. A. Shoitov, and A. I. Yuzhin, *Sov. Phys. Solid State* **26**, 923 (1984).
- <sup>45</sup>A. A. Benditskii, L. V. Viduta, Yu. A. Kulyupin, A. P. Ostranitsa, P. M. Tomchuk, R. D. Fedorovich, and V. A. Yakovlev, *Bull. Acad. Sci. USSR, Phys. Ser. (Engl. Transl.)* **50**, 170 (1986).
- <sup>46</sup>A. A. Benditskii, L. V. Viduta, B. I. Konov, S. M. Pimenov, A. M. Prokhorov, P. M. Tomchuk, R. D. Fedorovich, N. I. Chapliev, and V. A. Yakovlev, *Poverkhn.: Fiz., Khim., Mekh.* **10**, 48 (1988).
- <sup>47</sup>L. V. Keldysh, *Sov. Phys. JETP* **20**, 1307 (1964).